Journal of Materials Chemistry A

PAPER

View Article Online
View Journal | View Issue

Cite this: J. Mater. Chem. A, 2018, 6, 17751

Nitrogen- and sulfur-enriched porous carbon from waste watermelon seeds for high-energy, high-temperature green ultracapacitors†

Ranjith Thangavel,[a] Aravindaraj G. Kannan,[b] Rubha Ponraj,[b] Vigneysh Thangavel,[c] Dong-Won Kim[b] and Yun-Sung Lee*[a]

Electrochemical ultracapacitors exhibiting high energy output and an ultra-long cycle life, utilizing green and sustainable materials, are of paramount importance for next-generation applications. Developing an ultracapacitor that has high output energy under high power conditions in a high-voltage non-aqueous electrolyte and maintaining a long cycle life is an ongoing challenge. Herein, we utilize watermelon seeds, a bio-waste from watermelons, for use in high-voltage, high-energy, and high-power ultracapacitors in a sodium ion-based non-aqueous electrolyte. The as-synthesized hierarchically porous, high surface area carbon is surface-engineered with a large quantity of nitrogen and sulfur heteroatoms to give a high specific capacitance of ~252 F g^{-1} at 0.5 A g^{-1} and 90 F g^{-1} at 30 A g^{-1}. An ultra-high stability of ~90% even after 150 000 cycles (10 A g^{-1}) with 100% coulombic efficiency is achieved at room temperature (25 °C), equivalent to an ultra-low energy loss of ~0.0667% per 1000 cycles. Furthermore, the porous carbon demonstrates remarkable stability even at high temperature (55 °C) for 100 000 cycles (10 A g^{-1}), ensuring the safety of the device and enabling it to outperform graphene-based materials. A maximum energy of ~79 W h kg^{-1} and a maximum power of 22.5 kW kg^{-1} with an energy retention of ~28.2 W h kg^{-1} was attained. The results provide new insights that will be of use in the development of high-performance, green ultracapacitors for advanced energy storage systems.

Received 4th June 2018
Accepted 29th August 2018

DOI: 10.1039/c8ta05248d

rsc.li/materials-a

1. Introduction

Recent scientific advances have promoted the use of energy storage devices (EES) in power hybrid vehicles (EVs) and hybrid EVs (HEVs).[1] High-performance EES supplying simultaneous high energy and high power are of key importance in such next-generation devices.[2] Although high-energy batteries have emerged as prime candidates for EVs and HEVs, their limited capabilities cannot satisfy the huge power requirements of these vehicles.[3,4] A device capable of providing higher power is crucial for cases where batteries fail to work.

Supercapacitors (also known as ultracapacitors) are promising substitutes for batteries under high-power conditions. Unlike batteries, where ion storage occurs through diffusion into the bulk of an active material, capacitors store ions over the surface of the active material.[5,6] Supercapacitors achieving charge storage at the electrode–electrolyte interface by non-faradic surface adsorption are termed electrical double-layer capacitors (EDLCs), while those in which charge storage occurs by faradic surface pseudocapacitance are termed pseudocapacitors.[7]

EDLCs are the more attractive option from a commercial point of view, owing to their simpler construction utilizing porous carbon, their high power, and their extraordinary cycle life (>10^6) compared with pseudocapacitors.[8,9] The expensive and complex inorganic metal oxides used in pseudocapacitors undergo continuous structural deterioration, which is not favorable for long-term applications; thus, most research efforts are now directed towards EDLCs, in which there is almost no structural change.[10,11] The major hurdles EDLCs currently face are: (i) choice of porous carbon, which should have a large number of accessible pores to store even large sized solvated ions from non-aqueous electrolytes, and deliver a high capacitance; (ii) low energy density, as incompatibility with organic/non-aqueous electrolytes over a large voltage window greatly minimizes the output energy and stability; and (iii) unsatisfactory power behavior, as high ion/electron movement resistance at high currents can lead to failure of the capacitor.[12,13]

Porous activated carbons (ACs) derived from coal and pitch are commercially used for EDLCs; however, scarcity of fossil fuels and the poor conductivity and low capacitance of ACs limit large-scale implementation.[14–16] Ordered mesoporous carbons,

[a]Faculty of Applied Chemical Engineering, Chonnam National University, Gwang-ju 500-757, Republic of Korea. E-mail: leeys@chonnam.ac.kr

[b]Department of Chemical Engineering, Hanyang University, Seoul 04763, Republic of Korea

[c]School of Electrical and Electronics Engineering, SASTRA University, Thanjavur, India

† Electronic supplementary information (ESI) available. See DOI: 10.1039/c8ta05248d

polymer-derived carbons, carbide-derived carbons, carbon nanotubes, carbon nanofibers, aerogels, metal–organic framework derived carbon, and graphene have all been intensively studied as alternatives for EDLC applications.[17–20] However, the tedious and high-cost manufacturing process obstructs the practical implementation of EDLCs based on such carbons. A promising alternative could be porous biomass-derived carbons.[21–23] Every year, millions of tonnes of industrial/household waste are generated; employing this waste in EES could help promote a clean and sustainable environment. The ready availability of biomass/waster precursors, potential for precise structural tuning of porous 3D morphology, and easy textural tailoring of these carbons are further advantages with respect to practical implementation.[24,25] The preparation of porous carbon from bio-mass precursor involves a simple chemical activation with pore forming agents such as KOH, H_3PO_4, $ZnCl_2$ and much more.[13] Metal oxide and metal hydroxides templates are also used for preparation of novel porous carbon nanosheets and graphene nanocapsules. Such carbon show a high surface area, and hierarchical short porosity with 3D interconnected networks.[9,18,25] However, utilization of biomass-derived carbons for high-energy, high-power capacitors is still in the nascent stage and requires further investigation.

To date, many EDLCs have involved aqueous electrolytes (1–1.2 V).[26–28] The limited voltage window weakens the energy output of a capacitor system, as energy density is directly proportional to working potential.[29,30] Ionic liquids (ILs) were recently shown to enable high-energy supercapacitors by extending the working voltage window of EDLCs. Despite this advantage, the large ions in ILs and their low viscosity severely undermine their output power and stability.[31,32] Additionally, the unfavorable reaction of ILs with carbon surface functionalities and their high cost obstruct the stability and the practical applications, respectively, of high-energy capacitors.[33,34] High stability is not possible even with a restricted voltage window (0–2.5 V), and so the quest for high-energy, high-stability capacitors continues. Although organic electrolytes have attracted considerable attention for use in commercial batteries, their applicability in high-energy EDLCs is still in the primary stage of research. A wide potential window (0–3 V), and the highly viscous nature, high ionic conductivity, and low cost of organic electrolytes could enable high-energy, high-power, and super-stable ultracapacitors to be built. However, to date, such high-energy ultracapacitors – and, in particular, the use of biomass-derived porous carbons – have not been deeply investigated with respect to improved performance.

An ideal ultracapacitor must deliver a high energy density under high power conditions. Much of the research to date has been devoted to improving the capacitance by structural modification, *i.e.*, increasing the surface area by providing well-interconnected mesopore channels.[35–37] Despite the favorable porous architecture, the poor electron flow in pore channels, poor electrode–electrolyte wettability, and ineffective ion adsorption over carbon pores at high current rates limit the performance of EDLC-based systems.[38–40] The surface functionalities of porous carbon play a dominant part in the efficient performance of EDLCs, by enhancing the accessible pore area for adsorption and electron flow, thereby delivering an enhanced capacitance. Additionally, favorable surface functionalities are essential to wet the carbon surface with the electrolyte and to achieve an excellent stability.[41–43]

Surface chemistry modification by introducing hetero atom doping is a versatile approach to improve the performance. Hetero atoms such as nitrogen, sulfur, boron, and phosphorous have been widely discussed with respect to aqueous EDLCs.[44,45] Recently, the strategy of dual hetero atom doping into carbon frameworks was demonstrated to enable superior performance in electro catalysis applications, but this has not been widely investigated for high-energy capacitors.[46,47] In particular, the influence of dual hetero atoms on the performance of high-energy organic electrolyte-based EDLCs has not yet been studied.

In this research, we develop for the first time a high-energy and robust ultracapacitor, utilizing waste watermelon seed-derived porous carbon in an inexpensive sodium ion-based organic electrolyte. Watermelons are widely consumed fruit throughout the world and the global production is more than 110 million tons per year. A large share of this production is consumed by agro-industries where disposal of waste watermelon seeds are a great issue. Employing such bio-waste towards development energy storage devices would be more economical and develop a green environment. Moreover, watermelon seeds contain a large quantity of amino acids that act as *in situ* source for heteroatoms during pore formation process. Moreover, the adsorption kinetics of bio-mass derived carbon are greatly enhanced by synergistic benefits of dual hetero atom (nitrogen and sulfur) surface functionalities. The ultracapacitors with surface-tuned porous carbon delivered an outstanding capacitance with a specific energy of ~22.5 kW kg^{-1} and a specific power of ~25 kW h kg^{-1}, with an ultra-low energy loss and an outstanding stability for 150 000 cycles. Significantly, an extraordinary stability for 100 000 cycles was documented at an elevated temperature (55 °C) even with a wide potential window (0–3 V), ensuring the safety of the device. The current research will enable the emergence of inexpensive next-generation ultracapacitors for practical applications.

2. Experimental section

2.1 Synthesis of WDCs and NS-WDCs

Watermelons were purchased from a local market in Korea, and the watermelon seeds were collected after removing the edible portions. The seeds were then washed several times with distilled water followed by ethanol, and then dried in an oven at 120 °C. The dried seeds were then well ground to powder, prior to the carbonization step. Carbonization was carried out in an Ar atmosphere at 600 °C for 2 h. The pore formation involved chemical activation with KOH; the ratio of carbon to KOH (Sigma Aldrich) was set to be 1 : 5 at 800 °C for 2 h, in an Ar atmosphere. The products were then washed with a 0.1 M HCl solution, followed by washing with distilled water and ethanol several times, and then dried to obtain WDC. For nitrogen and sulfur doping, thiourea was used as the source, and the mass

ratio of thiourea (Sigma Aldrich, 99%) to WDC was set at 1 : 1. The WDC and thiourea were mixed well and then annealed at 600 °C for 2 h. For a comparison, WDCs were also synthesized at 700 °C and 900 °C and the term "WDC" and "NS-WDC" stands for porous carbon obtained at 800 °C, unless otherwise stated.

2.2 Material characterization

TGA was performed in a thermal analyzer system (STA 1640, Stanton Redcroft Inc., UK). X-ray diffraction patterns of the samples were obtained using a Rigaku D/MAX 2500 diffractometer. The morphologies of the porous carbon materials were characterized using field emission scanning electron microscopy (FE-SEM, JEOL JSM 6701F) and high-resolution transmission electron microscopy (HRTEM, JEOL, JEM 2100F) equipped with energy dispersive spectroscopy (EDS). Nitrogen adsorption/desorption isotherm experiments were performed using an ASAP-2020, Micromeritics, USA apparatus at 77 K. The samples were degassed at 300 °C, 2 h under vacuum prior to the adsorption/desorption measurements. The micropore size distributions of the porous samples were determined based on non-local density functional theory (NLDFT) assuming a slit pore model, and mesopore distribution was based on the Barrett–Joyner–Halenda (BJH) model. Elemental analysis was carried out in a LECO CHNS microanalyzer. XPS (VG Multilab ESCA System, 220i) was used to confirm carbonization and to characterize the surface functional groups. Raman spectra of the carbon powders were recorded using a Dongwoo Optron, MonoRa 780i spectrometer. The electrical conductivities were determined using a four-pin probe apparatus (Loresta-GP MCP-T610, Mitsubishi Analytech) at 25 °C using a carbon pellet (1 cm diameter) pressed at 10 MPa.

2.3 Electrochemical characterization

The supercapacitor electrodes were formulated with the following composition: active material (80 wt%), Ketjen black (10 wt%) as conductive carbon, and teflonized acetylene black as binder (10 wt%). The electrode slurry was rolled and pressed over a stainless-steel mesh and the electrodes were then dried at 160 °C for 4 h in a vacuum oven. The mass loading of electrode was ~2.5–3.5 mg cm^{-2}, and the electrode density was calculated to be 0.58–0.6 g cm^{-3}. For the three-electrode electrochemical measurements, a single porous carbon electrode acted as the working electrode, platinum wire acted as the counter electrode, and $Ag/AgNO_3$ were used as the reference electrode with 1 M $NaClO_4$ in EC/DMC (1 : 1 vol/vol) electrolyte. For the two-electrode electrochemical measurements, two symmetrical porous carbon electrodes were placed in a standard CR2032 coin cell, separated by a porous polypropylene (Celgard 3401, USA) separator, and the cell was filled with 1 M $NaClO_4$ in EC/DMC (1 : 1 vol/vol) electrolyte. All the supercapacitor cells were assembled in an argon-filled glove box. Cyclic voltammetry (CV) and electrochemical impedance spectroscopy (EIS) were carried out in a Bio-Logic (SP-150, France) workstation. Galvanostatic studies were performed between 0 and 3 V using a Won-A-Tech (WBCS 3000, Korea) battery cycler. The specific capacitance of each electrode was calculated based on the formula C_s (F g^{-1}) = $2(I \times t)/(V \times m)$, where I is the applied current (A), t is the discharge time (s), V is operating voltage (V), and m is the mass in each electrode (g). Since two symmetrical electrodes were employed in the supercapacitors, the energy density of the supercapacitor was calculated as $E = (CV^2/8)$ W h kg^{-1}, and the power density was calculated as $P = (E/t)$ kW kg^{-1}.

3. Results and discussion

3.1 Structural & textural characterization of WDCs

In the search for renewable resources for green and sustainable EES, watermelon seeds are an abundant and attractive biomass resource. Watermelon seed is a rich source of carbon, hydrogen, and various amino acids, and therefore has potential for *in situ* hetero atom doping and the synthesis methodology is given in Scheme 1. Thermogravimetric analysis (TGA) was carried out to analyze the carbonization of the watermelon seeds. The TGA curve in Fig. S1† shows an initial weight loss between 100 and 200 °C, which can be attributed to the removal of moisture. The weight loss between 200 and 600 °C indicates the removal of CO_2 and CO owing to the escape of H and O atoms from watermelon seeds and the formation of a carbonized product.[48] The yield of the carbonization process was ~22%; such a simple and low-cost carbonization process is highly suitable for industrial-scale production. The subsequent pore formation step utilizing KOH chemical activation involves a relatively lower temperature (800 °C) and a short time (2 h).[48] The conventional activated carbons are synthesized from coal and coke precursors by a tedious and expensive physical activation technique utilizing steam or CO_2 at a high temperature (1200 °C). As a result, the lower energy consumption and higher yield of carbon when utilizing this eco-friendly green resource are highly favorable for scaling up the process for industrial production.

The porous structure of pristine watermelon seeds derived porous carbon (WDC) and nitrogen-sulfur enriched watermelon seeds derived porous carbon (NS-WDC) was analyzed by scanning electron microscopy (SEM) and transmission electron microscopy (TEM). The SEM image of pyrolyzed carbon prior to activation shown in Fig. 1a illustrates the irregular and rough lamellar surface, with no pores and cavities over it. However, after activation, WDC and NS-WDC develop huge numbers of randomly distributed pores over their surfaces (Fig. 1b and c, and S2†). This abundant pore formation is due to the evolution of gases such as H_2 and CO_2 as a result of carbon lamellae upon decomposition of KOH at high temperatures. The TEM images of WDC and NS-WDC shown in Fig. S2c† and 1d, respectively. The TEM images confirm the presence of randomly disturbed, worm-like, irregularly shaped pores, mainly in the micropore size region. The high-resolution TEM image of WDC and NS-WDC shown in Fig. S2† and 1e, respectively. The HR-TEM images illustrates the absence of any graphitic domains, indicating the amorphous nature of WDC. The energy-dispersive X-ray spectroscopy (EDAX) mapping of NS-WDC (Fig. 1f) clearly shows the random distribution of nitrogen and sulfur hetero atoms over the porous carbon. The X-ray diffraction patterns of WDCs synthesized at different temperature and NS-WDC are shown in Fig. S3a and

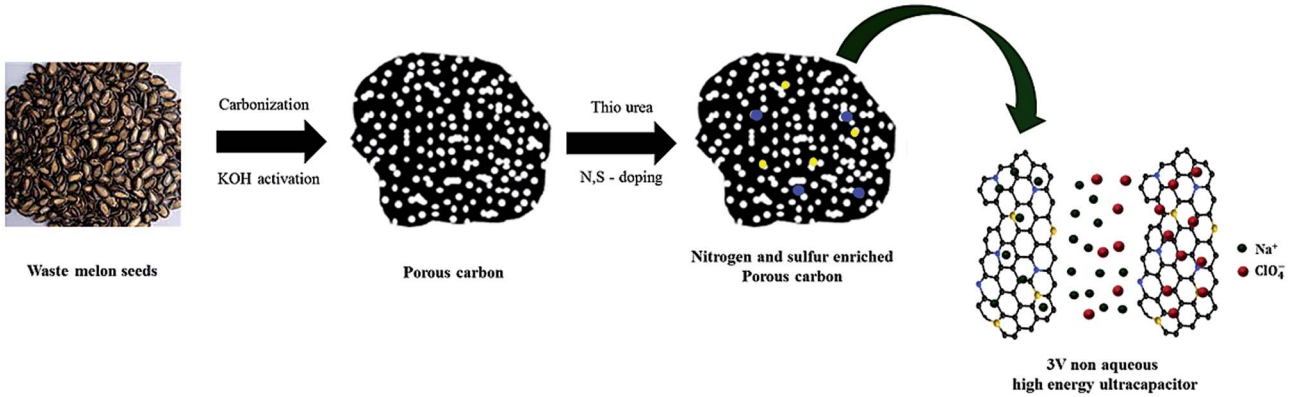

Scheme 1 Synthesis of nitrogen and sulfur enriched porous carbon from waste watermelon seeds.

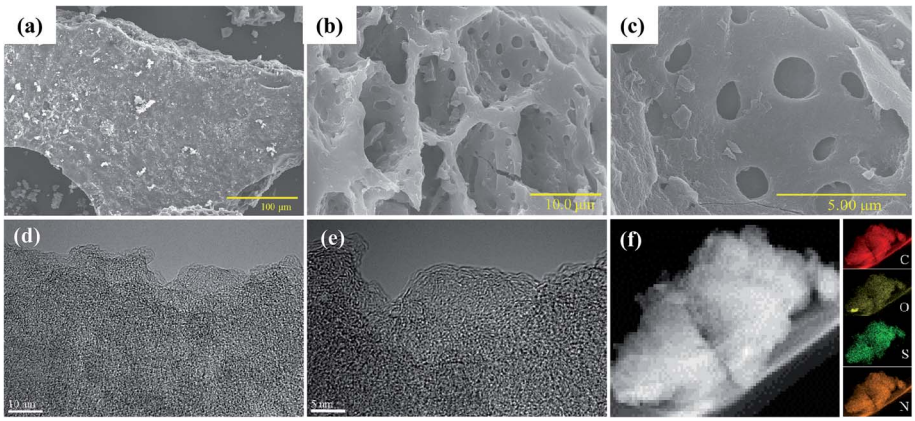

Fig. 1 (a) SEM image of carbonized watermelon seeds, (b and c) SEM images of WDC, (d and e) TEM images of NS-WDC, and (f) TEM-EDAX images of NS-WDC.

b† respectively. The two broad peaks around $2\theta = \sim 22°$ and 44° correspond to the (002) and (100) planes of graphitic carbon and the barely discernable peaks indicate the highly amorphous and disordered nature of porous carbon.[49]

Fig. 2a shows the N_2 adsorption/desorption isotherm of WDCs synthesized at different temperatures (700 °C, 800 °C, and 900 °C). WDC (700 °C) shows type I isotherm, indicating the micropores nature of the carbon with a surface area of ~1920 $m^2\ g^{-1}$ with a pore volume. WDCs synthesized at 800 °C shows a combination type I/IV isotherm with sharp knees in the low pressure region owing to strong adsorption on micropores, followed by a hysteresis indicating the presence of mesopores.[50,51] The BET surface area of WDC was calculated to be ~2383 $m^2\ g^{-1}$, with a pore volume of 2.28 $cm^3\ g^{-1}$. WDC (900 °C) also shows a combination type I/IV isotherm but the surface area and pore volume drops to ~2120 $m^2\ g^{-1}$ and 1.6 $cm^3\ g^{-1}$. As shown by the DFT pore size distribution curve (inset: Fig. 2a), most pores were smaller mesopores of less than 4 nm in size, with major pores ranging between 2–3 nm. The average pore size of WDC (700 °C), WDC (800 °C), and WDC (900 °C) were 1.87 nm, 2.3 nm, and 2.1 nm respectively. Increasing the activation temperature from 700 °C to 800 °C generates a huge amount of gas (CO, and CO_2) from activation agent (KOH) that favorably increases the textural properties. But further increasing the activation temperature to 900 °C makes the pores to collapse, unfavorably reducing the textural properties. The N_2 adsorption/desorption isotherms of NS-WDC were similar to WDC (800 °C), (Fig. S3c†), indicating that the textural properties are not modified after hetero atom doping. The surface area and pore diameter of NS-WDC is nearly similar as WDC (800 °C) as hetero atom doping with thiourea at 600 °C alter only the chemical nature of WDCs and not the textural properties. High porosity greatly maximizes the ion adsorption sites, thereby favoring high capacitance and providing quick electrolyte diffusion into deeper pores.[52] Owing to a high surface area, large pore volume along with the co-existence of hierarchical micro- and mesopores, WDCs synthesized at 800 °C can enable fast ion movement and favors accommodation of large solvated ions than other two counterparts.[53]

The Raman spectra of WDC synthesized at different temperatures in Fig. S3d† exhibited two major peaks at ~1350 cm^{-1} and ~1601 cm^{-1}, corresponding to the D band and G band. The G band originates from graphitic in-plane stretching from sp^2 carbon and the D band corresponds to defects and disorders in the carbon structure, originating from disordered carbon atoms with dangling bands. The I_D/I_G

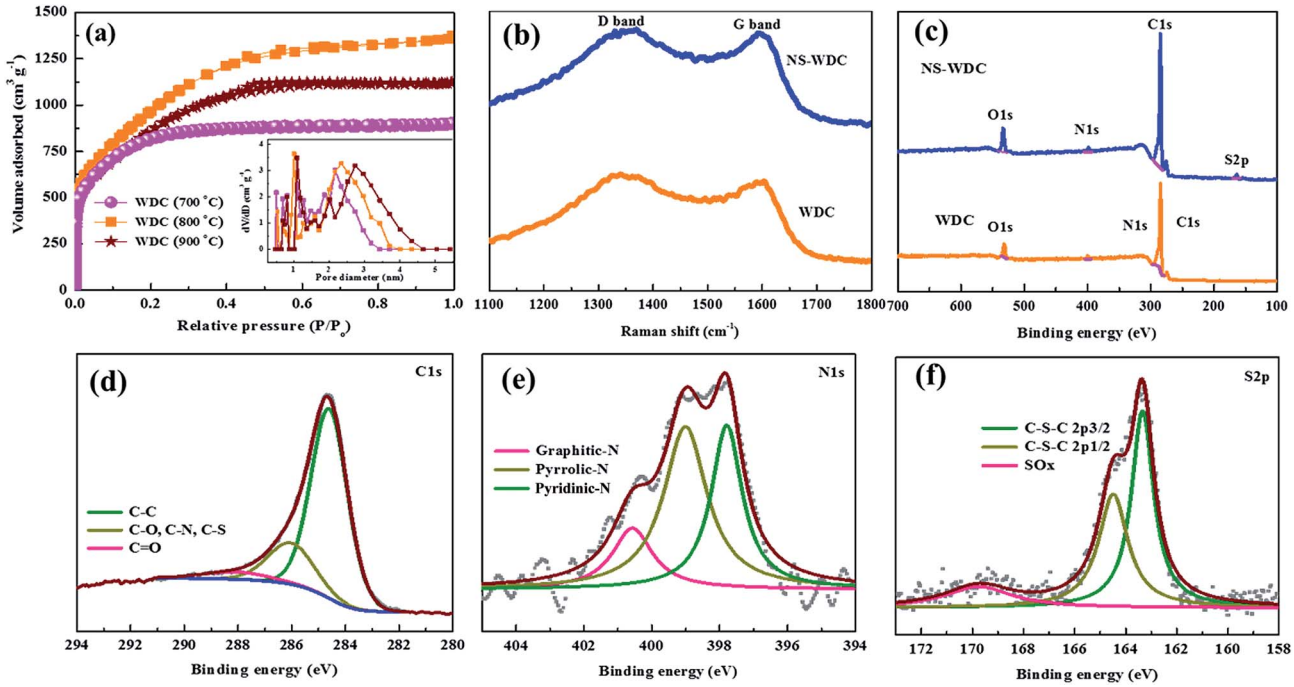

Fig. 2 (a) N_2 adsorption/desorption isotherm of WDCs synthesized at different temperature; inset: NLDFT pore size distribution, (b) Raman spectra of WDC and NS-WDC, (c) XPS survey spectra, and high-resolution XPS spectra of NS-WDC (d) C 1s, (e) N 1s, (f) S 2p.

intensity ratios for WDC synthesized at 700 °C, 800 °C, and 900 °C were calculated to be ~1.01, 1.02 and 0.99, respectively. The graphitization intensity gradually becomes weaker on increasing temperature from 700 to 800 °C, and then turns slightly stronger at higher temperature (900 °C). And so, a higher activation temperature may affect the performance of the porous carbon. The Raman spectra of NS-WDC in Fig. 2b exhibited the D-band at ~1350 cm^{-1}. However, the G band of NS-WDC shows a more redshift to ~1590 cm^{-1} compared to pristine WDC (1601 cm^{-1}). Such a redshift is attributed to n-type substitutional doping of porous carbon, confirming the heteroatom doping into the carbon framework.[38] The I_D/I_G intensity ratios for WDC and NS-WDC were calculated to be ~1.02 and 1.04, respectively.[54,55] These high values indicate the highly disordered nature of WDC after KOH activation and hetero atom doping. The mean electrical conductivities of WDC and NS-WDC, as measured by a four-probe technique, were ~1.1 and 5.1 S cm^{-1}, respectively, higher than that of commercial activated carbon available in market. The increases in electrical conductivity after hetero atom dopant is due to broadening of van-Hove singularities in the density of states making the Fermi level to shift towards conduction bands.[1]

3.2 Chemical composition of WDCs

Tables S1 and S2† shows the bulk and surface composition of WDC and NS-WDC as deduced by elemental analysis and X-ray photoelectron spectroscopy (XPS), respectively. Significant amounts of nitrogen hetero atoms were incorporated in WDC during the activation process, but sulfur hetero atoms were not present. In NS-WDC, more nitrogen and sulfur hetero atoms could be observed after activation with thiourea. The surface functionalities and incorporation of N and S hetero atoms in WDC were studied by XPS. The survey spectrum of WDC in Fig. 2c reveals the presence of carbon, oxygen, and nitrogen elements. Other possible metal impurities from biomass source were below the detection limit; these could have been removed during the post-acid washing process. The large amounts of nitrogen-containing minerals and amino acids in the watermelon seeds could aid *in situ* doping of nitrogen into the carbon framework during activation. The survey spectrum of NS-WDC in Fig. 2c confirms the presence of carbon, oxygen, nitrogen, and sulfur after the doping process. The quantities of nitrogen and sulfur after the doping process were ~4.13 and 3.31 wt%, respectively. To understand the chemical nature of dopants in NS-WDC, the C 1s, N 1s, and S 2p spectra were deconvoluted; the deconvoluted C 1s spectrum (Fig. 2d) shows three strong peaks at ~284.6, 285.7, and 289.1 eV. The peak at ~284.6 eV originated from the C–C bond of sp^2-hybridized carbon, confirming the highly carbonaceous nature of the material. The peaks at ~285.7 and ~289.1 eV originated from C–O, C–S, and C–N functional groups and carboxyl functional groups, respectively. The deconvoluted N 1s core level spectrum in Fig. 2e shows three contributions from pyridine (~398.3 eV), pyrrole, and pyridone (~399.8 eV), and quaternary (~401.1 eV).[43] The S 2p peak (Fig. 2f) can be resolved into two major contributions from $2p_{3/2}$ and $2p_{1/2}$ components, corresponding to non-oxidized forms of sulfur bonding in aromatic carbon frameworks (C–S–C). The minor contribution from ~169 eV is associated with the oxidized state (C–SO_x) of sulfur atoms.[38,56] This result confirms the successful incorporation of nitrogen and sulfur hetero atoms into WDC carbon frameworks. A large

quantity of hetero atoms in a carbon framework can provide a large number of active sites for adsorption. Additionally, the conductivity and surface wettability by electrolyte increases with the increasing presence of hetero atoms, which is favorable for efficient ion adsorption at high current rates.[57,58]

3.3 Supercapacitor performance

The electrochemical performance of porous carbon was studied with an organic electrolyte based on sodium ions ($NaClO_4$) in ethylene carbonate/dimethyl carbonate (EC/DMC) to achieve a wide operating window and thereby achieve a high energy density.[31,59] The weaker solvation of sodium ions due to its weaker acidity can favor high ion transfer kinetics and a higher transport number than the conventional lithium analogues.[60] The electrochemical performances of WDC and NS-WDC were briefly analyzed in symmetrical two-electrode configurations. Performance evaluation by a symmetrical two-electrode system is an effective means of assessing the practical performance of the material, as the potential applied is shared equally between two electrodes. However, in three-electrolyte configurations, the single working electrode takes all the applied potential and shows an exaggerated capacitance value; hence, such evaluations do not provide the true metrics of a material (the performance of WDC in a three-electrode configuration is shown in Fig. S4†). In general, with a three-electrode configuration, porous carbon materials show higher discharge times than those obtained in two-electrode configurations.[61,62]

The CV curves of WDC and NS-WDC in a symmetrical two-electrode configuration (Fig. S5†) exhibited perfect rectangular shapes, indicating the ideal characteristics of EDLCs.[63] No redox peaks/humps due to the pseudocapacitive interaction of ions with functional groups were observed. The pseudocapacitance behavior in porous carbon strongly depends on nature of the electrolytes (ex: type and pH) and the effect is almost negligible in neutral and non-aqueous electrolytes.[1] Even with an increase in scan rate, both WDC and NS-WDC maintained perfect rectangular-shaped profiles, indicating faster kinetics in the porous carbon due to the openness in structure favoring fast ion transportation inside the pores. At 100 mV s^{-1}, the CV curves of NS-WDC still maintained the EDLC shape along with a large output current, while WDC deviate from the rectangular profile (Fig. 3a). This is due to an increase in ion transport and ion adsorption kinetics of NS-WDC after hetero atom doping.[64] Along with these faster kinetics, NS-WDC can deliver a remarkable rate performance compared with that of WDC.

The charge–discharge (CD) curves of WDC and NS-WDC showed a highly symmetrical and linear triangular shape profile, again confirming the pure double-charge storage reaction in capacitors (Fig. 2b–d). At 0.5 A g^{-1}, WDC exhibited a specific capacitance of ~249 F g^{-1} and NS-WDC delivered a specific capacitance of 252 F g^{-1} (Fig. 2b). The surface area of both WDC and NS-WDC is almost identical with similar pore distribution and so delivered almost a same capacitance. The specific capacitance of supercapacitor device is greatly depends on efficient utilization of pores for double layer formation by ions. A low current density of 0.5 A g^{-1}, where the resistance between electrodes are negligible and ions in electrolyte have large time to access all the pores for double layer formation. The electrochemical performance of WDC (700 °C) and WDC (900 °C) are also evaluated (Fig. S6†) and they delivered a specific capacitance of ~210 F g^{-1} and 231 F g^{-1} at 0.5 A g^{-1}

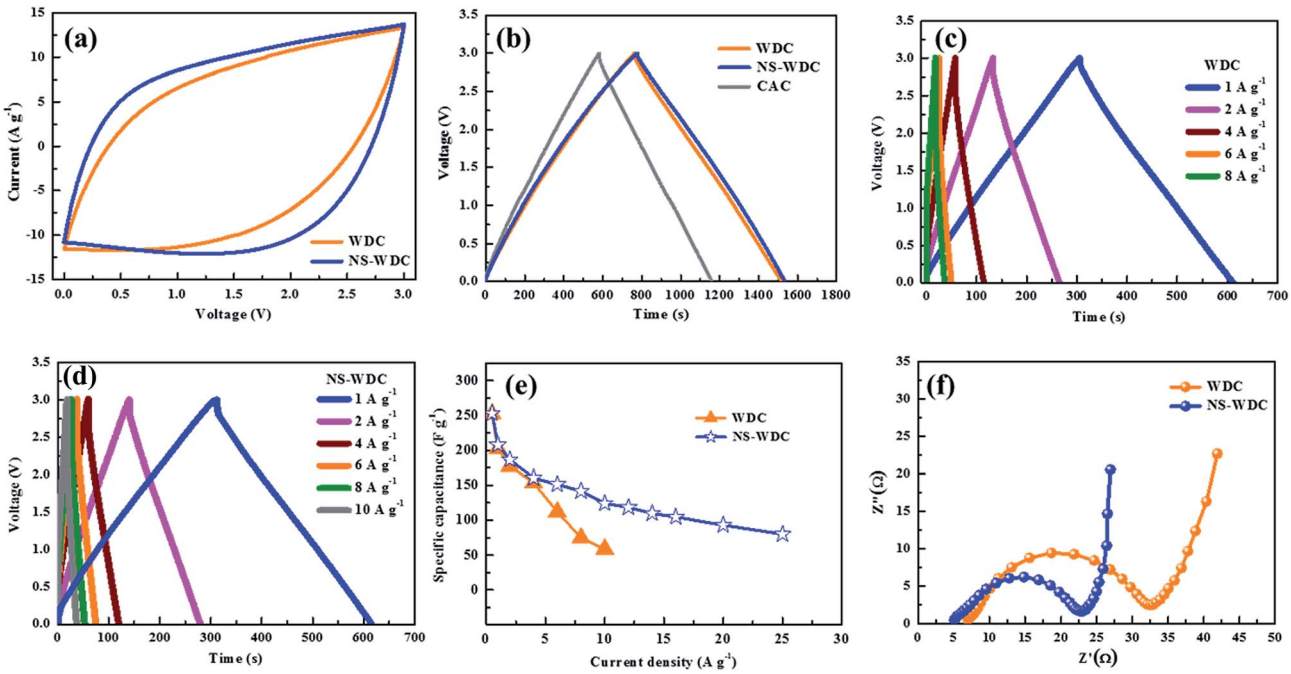

Fig. 3 (a) CV curves of WDC and NS-WDC at 100 mV s^{-1}, (b) CD curves at 0.5 A g^{-1}, (c) CD curves of WDC, (d) CD curves of NS-WDC, (e) rate performance of WDC, and NS-WDC, and (f) Nyquist plots of WDC and NS-WDC supercapacitors.

respectively, lower than WDC (800 °C). The capacitances delivered by WDC and NS-WDC are the highest reported for biomass-derived porous carbon with organic electrolytes, and they outperform commercial ACs and template-derived carbons. The high capacitance can mainly be attributed to the extremely high surface area of the carbon and the presence of large numbers of pores after the activation process that are easily accessed by electrolyte ions.[65,66] The large number of highly accessible pores favors fast ion movement to deliver a high capacitance. The extremely large number of pores in the WDC equivalent of the electrolyte ion size provides sites for ion adsorption.[67,68] For comparison, commercial activated carbon (N_2 adsorption/desorption isotherms shown in Fig. S7,† surface area: 1895 m^2 g^{-1}) was also tested under similar conditions, and exhibited a low discharge time with poor specific capacitance of ~185 F g^{-1} at 0.5 A g^{-1} (Fig. 2b). The highly microporous commercial activated carbon is not favorable for accommodating ions from non-aqueous electrolytes. The macropores generally function as ion transport channels, helping the ions to move deeper into micro- and mesopores for efficient double-layer formation.[69]

The rate performances of WDC and NS-WDC are shown in Fig. 3e. Although the specific capacitances delivered by WDC and NS-WDC were nearly the same at lower current densities, the discharge times and specific capacitances varied markedly at higher current rates. WDC delivered a specific capacitance of ~203 and 59 F g^{-1} at 1 A g^{-1}, and 10 A g^{-1}, respectively, much higher than WDC (700 °C) and WDC (900 °C) as shown in Fig S6.† The low performance of WDC (700 °C) and WDC (900 °C) than WDC (800 °C) is attributed to smaller surface area and small pore size of the former, limiting the kinetics of the ion adsorption process. NS-WDC delivered a high capacitance of ~208 and 124 F g^{-1} at 1 A g^{-1} and 10 A g^{-1}, respectively. Even at a high current density of 25 A g^{-1}, where WDC failed to work, NS-WDC delivered a capacitance of ~80 F g^{-1} – much higher than that obtained for WDC at 10 A g^{-1}. In general, a high capacitance at a high current rate can be easily obtained in aqueous electrolytes with a small potential window, but it is hard to realize high capacitance with non-aqueous electrolytes where ion movement is much more restricted, even with a wider potential window.[70,71] However, a superior capacitance was achieved in NS-WDC after chemical modification of pores with hetero atoms. The capacitance at high current densities surpasses that of several previously reported carbons such as hierarchal porous carbon, 3D graphene, bimodal carbon, CNTs, carbon monoliths, and other biomass-derived carbons.[5,13,18,19,24,28,56] The effects of the carbon : thiourea ratio on the total number of hetero atoms doped and the output capacitance were also analyzed. The elemental analysis (Table S3†) shows that with a carbon : thiourea mass ratio of 1 : 0.5, the amount of nitrogen and sulfur was smaller than that obtained with a ratio of 1 : 1. Increasing the ratio to 1 : 2 increased the amount of nitrogen doped but decreased the amount of sulfur, while the total number of hetero atoms remained nearly the same. The specific capacitance of NS-WDC obtained with other hetero atom contents was inferior to that of NS-WDC made with a carbon : thiourea mass ratio of 1 : 1 (Fig. S8†).

The superior capacitive performance of NS-WDC over WDC, despite a similar surface area, and pore size can be mainly attributed to the synergistic effects of the large numbers of nitrogen and sulfur hetero atoms in carbon frameworks. The dual hetero atoms greatly modified the chemical and surface nature of the porous carbon, leading to a superior performance. Hetero atoms are well known to improve the ion and electron transfer kinetics of carbon. To further understand these effects, impedance spectroscopy studies were carried out for WDC and NS-WDC (Fig. 3e). The Nyquist plots of both samples show an initial solution resistance, a semi-circle in the high-frequency region that can be ascribed to charge transfer resistance

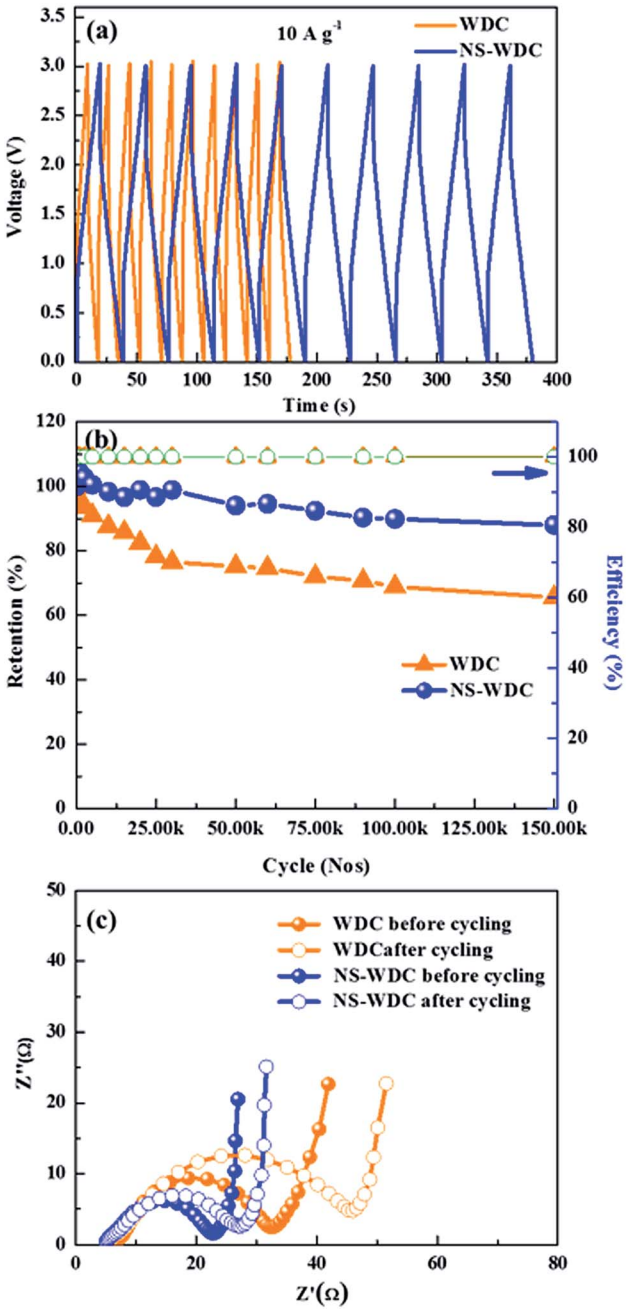

Fig. 4 (a) Continuous CD profile of WDC and NS-WDC at 10 A g^{-1}, (b) cyclic stability of WDC, and NS-WDC at 10 A g^{-1}, (c) Nyquist plots of WDC and NS-WDC before and after cycling.

originating from electronic and ionic conductivity of the carbon electrode, and a Warburg tail at low frequency indicating a capacitive-type storage. As can be clearly seen, the solution resistance was greatly reduced after the incorporation of nitrogen and sulfur hetero atoms, indicating an improved electrode–electrolyte interface.[31] Furthermore, NS-WDC showed a smaller charge transfer resistance than WDC, owing to its highly porous nature along with the heavily doped hetero atoms that promote rapid ion transfer kinetics.

The graphitic N in NS-WDC greatly improves electron transport by decreasing the intrinsic resistance, and the pyridinic and pyrrolic N in porous carbon strongly favors rapid ion transport kinetics inside the pores. The sulfur hetero atoms can greatly enhance space utilization by promoting the electrosorption of electrolyte ions.[14,25] The presence of hetero atoms increases the polarity of the pores and thereby facilitates easy contact between pore and electrolyte. Additionally, the surface wettability nature of S-WDC is greatly enhanced by sulfur atoms, thereby reducing the interface resistance between electrode and electrolyte and overcoming the ion diffusion losses.[14,25] This promotes easy ion diffusion into pores even at high current densities and thus delivers a high capacitance. Under high-current conditions in WDC, the high ohmic resistance inside the micropores could led to an ion "traffic jam" effect and hence a reduced capacitance. Although nitrogen heteroatoms are available in WDC, a smaller amount of heteroatoms do not significantly affect their electrochemical performance. However, in NS-WDC, the presence of dual hetero atoms greatly reduces such resistance and increases the pore utilization to achieve a high capacitance.[5] The contact angle measurements (Fig. S9†) showed that NS-WDC had better surface wettability with the electrolyte than WDC. The improved wettability allows the electrolyte to penetrate deeper into micropores, thereby allowing a greater pore area to participate in double-layer formation even at high current rates. The hierarchical macro-meso-micro pore arrangement further facilitates easy and

Table 1 Comparison of performance of various capacitor systems with those of the current work

Carbon type	Electrolyte	Potential	Specific capacitance	Stability	Energy density (W h kg^{-1})	Power density (kW kg^{-1})
NS-WDC (this work)	**1 M $NaClO_4$ in EC:DMC**	**0–3 V**	**252 F g^{-1} at 0.5 A g^{-1} (25 °C), 80 F g^{-1} at 25 A g^{-1} (25 °C), 90 F g^{-1} at 30 A g^{-1} (55 °C)**	**90% – 150 000 cycles**	**79**	**22.5**
WDC (this work)	**1 M $NaClO_4$ in EC:DMC**	**0–3 V**	**249 F g^{-1} at 0.5 A g^{-1} (25 °C), 59 F g^{-1} at 10 A g^{-1} (25 °C)**	**75% – 150 000 cycles**	**77.8**	**7.5**
Hemp derived carbon[5]	BMPY TFS, 99%	0–3 V	122 F g^{-1} at 1 A g^{-1}	96% – 10 000 cycles	50	12
N, S doped hierarchical porous graphene[47]	1M $LiPF_6$ in EC:EMC	0–3 V	147 F g^{-1} at 0.8 A g^{-1}	94.5% – 25 000 cycles	—	—
Polypyrrole derived carbon[71]	EMIM TFSI	0–2.3 V	120 F g^{-1} at 20 A g^{-1}	~95–96% – 10 000	—	—
High surface area bimodal carbon[37]	EMIM TFSI in AN	0–3 V	160 F g^{-1} at 1 A g^{-1}	85% – 10 000 cycles	60	
Pulp sludge derived porous carbon[32]	1.5 M $TEABF_4$/AN	0–3 V	163 F g^{-1} at 0.1 A g^{-1}	91% – 5000 cycles	51	7
3D graphics[33]	1 M $TEABF_4$/AN	0–2.7 V	202 F g^{-1} at 1 A g^{-1}	94% – 5000 cycles	51	—
Carbide derived carbon[34]	$EMIBF_4$	0–2 V	171 F g^{-1} at 0.1 A g^{-1}	10 000 cycles	—	—
Hierarchal porous carbon[11]	$LiClO_4$ in PC/DME	2–4 V *vs.* Li	120 F g^{-1} at 0.05 A g^{-1}	Not studied	—	—
CNTs[26]	$BMIMEF_4$	0–3 V	150 F g^{-1} at 5 A g^{-1}	80% – 4000 cycles	47	4.3
CNTs[26]	2.0 M H_2SO_4	0–1 V	172 F g^{-1} at 5 A g^{-1}	80% – 4000 cycles	6	1
Rice husk derived carbon[50]	1 M $NaSO_4$	0–1 V	112 F g^{-1} at 1 A g^{-1}	—	—	—
Lignin-derived carbon[63]	6 M KOH	0–1 V	196 F g^{-1} at 50 A g^{-1}	5000 cycles	8.1	2.26
N, O doped porous carbon[10]	6 M KOH	0–1.6 V	90 F g^{-1} at 50 A g^{-1}	97.5% – 20 000 cycles	30.3	9.7
N–carbon monoliths from PAN[27]	6 M KOH	0–1 V	216 F g^{-1} at 1 A g^{-1}	92% – 3000 cycles	—	—
Porous carbon sphere waste sugar[28]	6 M KOH	0–0.9 V	210 F g^{-1} at 1 A g^{-1}	89.6% – 5000 cycles	8.5	—
Waste printed circuit derived carbon[16]	6 M KOH	0–1 V	190 F g^{-1} at 1 A g^{-1}	86% – 2000 cycles	7.3	0.45
MgO template carbon from coal tar pitch[17]	6 M KOH	0–1 V	224 F g^{-1} at 0.1 A g^{-1}	98% – 1000 cycles	7.8	—

rapid kinetics to achieve a high capacitance.[19,72] Therefore, the enhanced performance of NS-WDC is attributed to the favorable chemical nature of NS-WDC rather than the textural properties.

Long-term cyclability is an essential property for ultracapacitors. Here, it was tested at 10 A g^{-1}. The continuous CD curves of WDC and NS-WDC (Fig. 4a) clearly showed that NS-WDC could store a large amount of charge with a higher discharge time than WDC. The ultracapacitors showed an impressive stability for 150 000 cycles even with a non-aqueous organic electrolyte. A capacitance retention of ~90% was achieved by NS-WDC, while WDC achieved only 75% of the initial capacitance (Fig. 4b). Generally, EDLCs exhibit a life expectancy of ~100 000 cycles even with aqueous electrolyte, and supercapacitors exhibit a stability of ~25 000 with non-aqueous electrolyte in a restricted working potential (0–2.5 or 0–2.7 V). However, the present ultracapacitors delivered a remarkable stability for 150 000 cycles with 100% coulombic efficiency, even under high current densities with a non-aqueous electrolyte within a 3 V working potential window. Such robust stability means the current system outperformed several biomass-derived porous carbons, activated graphene, carbon nanotubes, carbon nanofibers, hard template carbons, and 3D ordered mesoporous carbon.[19,21,31,43,57,73–75] To further demonstrate the superior stability, Nyquist impedance was measured after cycling (Fig. 4c). Clearly, even after cycling, both WDC and NS-WDC showed a semicircle in the low-frequency region, followed by a Warburg tail. However, the solution resistance and charge transfer change for NS-WDC were much smaller than those for WDC after cycling, evidencing an active adsorption/desorption on the pores of the NS-WDC. The replacement of a large number of oxygen functionalities with favorable nitrogen and sulfur hetero atoms indicates greater affinity towards pore utilization for the continuous double-layer formation. Additionally, the pseudocapacitance contributions from N and S doping are not induced with organic electrolyte in ultra-high-surface-area carbons. The absence of such faradic reactions helps to maintain the surface nature of the pores, thereby maintaining the capacitance for more cycles.[47] Table 1 compares the output performances of WDC and NS-WDC with those of several previously reported carbons; the superiority of NS-WDC can be clearly observed.

The performance of NS-WDC was further evaluated at a higher temperature (55 °C), which confirms the safety of the ultracapacitors. The CV curves (Fig. 5a) remained perfectly rectangular even at elevated temperatures, indicating a facile and smooth adsorption/desorption process. The CD curve of NS-WDC at 55 °C shown in Fig. S10† perfectly maintains the triangular shape profile. At 1 A g^{-1}, NS-WDC delivered a specific capacitance of ~210 F g^{-1}, equivalent to the performance obtained at room temperature. However, at higher current densities, NS-WDC delivered a higher capacitance than that obtained at room temperature (Fig. 5b); this was ascribed to enhanced ionic conductivity at higher temperatures, facilitating fast ion transfer kinetics.[5] At 10 A g^{-1}, a specific capacitance of ~151 F g^{-1} was obtained, and even at 30 A g^{-1}, a specific capacitance of ~90 F g^{-1} was possible. This superior performance at high current density was mainly due to reduced electrode–electrolyte resistance, and enhanced ion flow between the pores and electrolyte at the higher temperature. The reduced resistance and enhanced ion kinetics are illustrated by the Nyquist plots

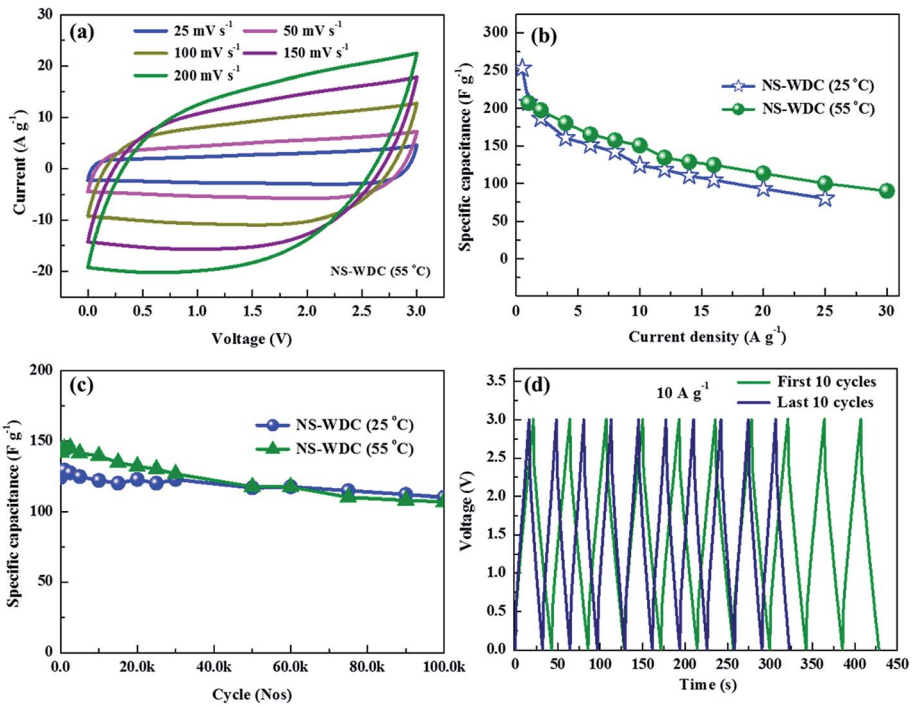

Fig. 5 (a) CV curves of NS-WDC at 55 °C, (b) rate performance of NS-WDC at 25 °C and 55 °C, (c) cyclic stability of NS-WDC at 10 A g^{-1} (55 °C), and (d) continuous CD profile of NS-WDC at 10 A g^{-1} during initial and last cycles (55 °C).

obtained at 55 °C (Fig. S11†), in which the solution resistance, electrolyte–electrode interface resistance, and charge transfer resistance can be seen to have been greatly reduced by the enhanced ionic conductivity of the electrolyte.[71]

A robust stability at high temperatures is the most important factor for ultracapacitors, and many systems fail to perform adequately under high-temperature conditions. However, NS-WDC showed superior capacitance retention for 100 000 cycles even at 55 °C with ~100% coulombic efficiency, comparable to the specific capacitance retention obtained at room temperature (Fig. 5c). The continuous CD curves of NS-WDC at elevated temperature during the first 10 cycles and final 10 cycles (100 000th) are shown in Fig. 5d; it can be seen that the triangular shape profile is well retained even after robust cycling, with negligible change in polarization and discharge time. Such a high stability with a non-aqueous organic electrolyte at elevated temperatures has never been reported to our knowledge. This ultra-stability was mainly ascribed to the highly stable nature of the electrolyte at elevated temperatures, even with a wide potential window (3 V). In addition, the nitrogen- and sulfur-containing functional groups over the pores could hold the electrolyte for a longer time, acting as a reservoir and aiding the continuous formation of the double layer.[47] The mechanically strong carbon frameworks of NS-WDC can also withstand continuous harsh charge–discharge conditions without structural damage.

3.4 Energy–power behavior of supercapacitor

To demonstrate the superiority of the biomass-derived porous carbon, a Ragone plot (Fig. 6) was constructed to compare the energy–power behavior with that of other energy storage systems. Based on the active mass in both electrodes, NS-WDC ultracapacitors delivered an ultra-high energy density of ~79 W h kg^{-1}, which is the highest value ever reported for an ultracapacitor utilizing an inexpensive organic liquid electrolyte. Even at ultra-high gravimetric power of 18.75 kW kg^{-1}, NS-WDC retained a gravimetric energy of ~25 W h kg^{-1}. Although WDC delivered an energy density of ~78.8 W h kg^{-1} at low power, it could only retain ~18.4 W h kg^{-1} of its energy at 7.5 kW kg^{-1}. At elevated temperatures, NS-WDC can function efficiently even at an ultra-high power density of ~22.5 kW kg^{-1}, with an energy density of ~28.2 W h kg^{-1}. Table 1 compares the energy behavior of the current system with that of several previously reported systems; it can be clearly seen that NS-WDC delivered a substantially higher energy and superior power. The superior energy–power output behavior effectively bridges the performance gap between batteries and capacitors. Based on the stability, the energy loss was calculated to be ~0.0667% per 1000 cycles, the lowest among the reported porous carbon materials. With such a low energy loss, the current system outperformed conventional EDLCs, hybrid capacitors, and batteries.[3,4] The stability was superior to that of several EES, making this system a promising candidate for use in EVs and HEVs.

To summarize, the superior capacitance, ultra-high rate capability, unparalleled stability at room temperature, and high temperature of the nitrogen and sulfur dual-doped porous

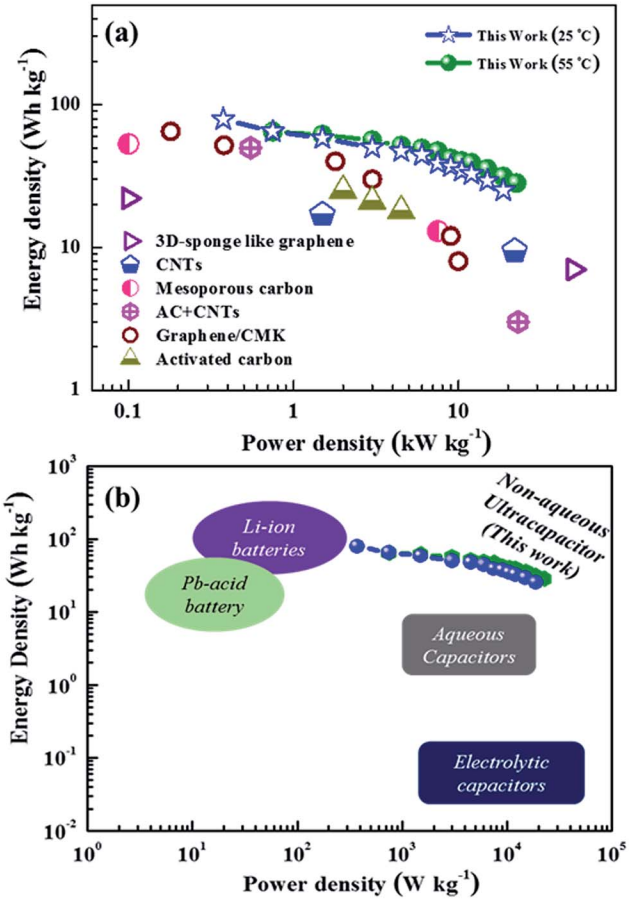

Fig. 6 (a) Ragone plots of WDC capacitors, (b) Ragone plot comparison with other capacitor systems.

carbon derived from watermelon seeds can be ascribed to the following factors: (i) the porous carbon with highly interconnected hierarchal pores yielded several active sites for ion adsorption/desorption reactions; (ii) the nitrogen and sulfur hetero atoms synergistically enhanced the electrical conductivity of the porous structure; (iii) the dual hetero atoms played a key part in improving the surface wettability of the electrodes with non-aqueous electrolytes, and greatly reduced the charge transfer resistance; (iv) the high mesopore content ensured electrolyte flow deep into the micropores and allowed rapid ion transport kinetics; (v) the strong carbon frameworks with reduced oxygen functionalities and macroporous electrolyte reservoir helped to achieve a ultra-strong stability; and (vi) the high compatibility of the non-aqueous electrolyte with NS-WDC over a wide working potential at elevated temperatures helped to maintain the porous structure without deterioration to achieve excellent stability under harsh conditions.

4. Conclusion

In summary, a simple and scalable method to produce porous carbon with interconnected hierarchical pores from a sustainable, low-cost, and widely available waste watermelon seed biomass precursor has been demonstrated. In addition, the

surface functionalities over the pore wall were tuned using nitrogen and sulfur hetero atoms to achieve excellent electrochemical performance even with non-aqueous electrolytes in a 3 V potential window. The electrochemical performance of the porous carbon was superior to that of conventional porous carbon and graphene-based electrodes. The stability and energy–power behavior were among the best reported for any porous carbon. A maximum energy density of 79 W h kg^{-1} was achieved, along with an ultra-high output power of ~22.5 kW kg^{-1}, while retaining an energy density of ~28.2 W h kg^{-1}. Furthermore, a long-lasting stability of 150 000 cycles with an energy loss of ~0.0667% per 1000 cycles was demonstrated, which is the lowest documented for any capacitor device. The superior stability at high temperatures (55 °C) for 100 000 cycles ensures the safety of the capacitor device, which thereby emerges as a strong competitor against conventional batteries and capacitors.

Conflicts of interest

We declare there are no conflicts to declare.

Acknowledgements

This work was supported by the National Research Foundation of Korea (NRF) grant funded by the Korea government (Ministry of Science, ICT & Future Planning) (No. 2016R1A4A1012224).

References

1 C. Zhong, Y. Deng, W. Hu, J. Qiao, L. Zhang and J. Zhang, *Chem. Soc. Rev.*, 2015, **44**, 7484–7539.
2 L. L. Zhang and X. S. Zhao, *Chem. Soc. Rev.*, 2009, **38**, 2520–2531.
3 J. R. Rani, R. Thangavel, S.-I. Oh, J. M. Woo, N. Chandra Das, S.-Y. Kim, Y.-S. Lee and J.-H. Jang, *ACS Appl. Mater. Interfaces*, 2017, **9**, 22398–22407.
4 R. Thangavel, B. Moorthy, D. K. Kim and Y.-S. Lee, *Adv. Energy Mater.*, 2017, **7**, 1602654.
5 H. Wang, *ACS Nano*, 2013, **7**, 5131–5141.
6 W. Qian, F. Sun, Y. Xu, L. Qiu, C. Liu, S. Wang and F. Yan, *Energy Environ. Sci.*, 2014, **7**, 379–386.
7 G. Zhao, J. Li, L. Jiang, H. Dong, X. Wang and W. Hu, *Chem. Sci.*, 2012, **3**, 433–437.
8 R. Thangavel, K. Kaliyappan, D.-U. Kim, X. Sun and Y.-S. Lee, *Chem. Mater.*, 2017, **29**, 7122–7130.
9 X. He, X. Li, H. Ma, J. Han, H. Zhang, C. Yu, N. Xiao and J. Qiu, *J. Power Sources*, 2017, **340**, 183–191.
10 D. He, J. Niu, M. Dou, J. Ji, Y. Huang and F. Wang, *Electrochim. Acta*, 2017, **238**, 310–318.
11 H. Yamada, I. Moriguchi and T. Kudo, *J. Power Sources*, 2008, **175**, 651–656.
12 M. S. Balathanigaimani, W.-G. Shim, M.-J. Lee, C. Kim, J.-W. Lee and H. Moon, *Electrochem. Commun.*, 2008, **10**, 868–871.
13 J. Ding, H. Wang, Z. Li, K. Cui, D. Karpuzov, X. Tan, A. Kohandehghan and D. Mitlin, *Energy Environ. Sci.*, 2015, **8**, 941–955.
14 Y. Ren, J. Zhang, Q. Xu, Z. Chen, D. Yang, B. Wang and Z. Jiang, *RSC Adv.*, 2014, **4**, 23412–23419.
15 D. Kai, M. J. Tan, P. L. Chee, Y. K. Chua, Y. L. Yap and X. J. Loh, *Green Chem.*, 2016, **18**, 1175–1200.
16 X. Du, L. Wang, W. Zhao, Y. Wang, T. Qi and C. M. Li, *J. Power Sources*, 2016, **323**, 166–173.
17 X. He, R. Li, J. Qiu, K. Xie, P. Ling, M. Yu, X. Zhang and M. Zheng, *Carbon*, 2012, **50**, 4911–4921.
18 X. He, H. Ma, J. Wang, Y. Xie, N. Xiao and J. Qiu, *J. Power Sources*, 2017, **357**, 41–46.
19 S. Rajendiran, K. Park, K. Lee and S. Yoon, *Inorg. Chem.*, 2017, **56**, 7270–7277.
20 H. Jiang, P. S. Lee and C. Li, *Energy Environ. Sci.*, 2013, **6**, 41–53.
21 V. Presser, M. Heon and Y. Gogotsi, *Adv. Funct. Mater.*, 2011, **21**, 810–833.
22 C. Guan, X. Xia, N. Meng, Z. Zeng, X. Cao, C. Soci, H. Zhang and H. J. Fan, *Energy Environ. Sci.*, 2012, **5**, 9085–9090.
23 Y. Liang, D. Wu and R. Fu, *Sci. Rep.*, 2013, **3**, 1119–1123.
24 M. Biswal, D. A. M. Banerjee and S. Ogale, *Energy Environ. Sci.*, 2013, **6**, 1249–1259.
25 G. Xu, J. Han, B. Ding, P. Nie, J. Pan, H. Dou, H. Li and X. Zhang, *Green Chem.*, 2015, **17**, 1668–1674.
26 H. M. Coromina, B. Adeniran, R. Mokaya and D. A. Walsh, *J. Mater. Chem. A*, 2016, **4**, 14586–14594.
27 Y. Wang, B. Fugetsu, Z. Wang, W. Gong, I. Sakata, S. Morimoto, Y. Hashimoto, M. Endo, M. Dresselhaus and M. Terrones, *Sci. Rep.*, 2017, **7**, 40259.
28 Z.-Q. Hao, J.-P. Cao, Y. Wu, X.-Y. Zhao, Q.-Q. Zhuang, X.-Y. Wang and X.-Y. Wei, *J. Power Sources*, 2017, **361**, 249–258.
29 M. M. Perez-Madrigal, M. G. Edo and C. Aleman, *Green Chem.*, 2016, **18**, 5930–5956.
30 F. Béguin, V. Presser, A. Balducci and E. Frackowiak, *Adv. Mater.*, 2014, **26**, 2219–2251.
31 R. Thangavel, A. G. Kannan, R. Ponraj, V. Thangavel, D.-W. Kim and Y.-S. Lee, *J. Power Sources*, 2018, **383**, 102–109.
32 H. Wang, Z. Li, J. K. Tak, C. M. B. Holt, X. Tan, Z. Xu, B. S. Amirkhiz, D. Harfield, A. Anyia, T. Stephenson and D. Mitlin, *Carbon*, 2013, **57**, 317–328.
33 L. Zhang, F. Zhang, X. Yang, G. Long, Y. Wu, T. Zhang, K. Leng, Y. Huang, Y. Ma, A. Yu and Y. Chen, *Sci. Rep.*, 2013, **3**, 1408.
34 M. Oschatz, S. Boukhalfa, W. Nickel, J. P. Hofmann, C. Fischer, G. Yushin and S. Kaskel, *Carbon*, 2017, **113**, 283–291.
35 Y. Li, Z. Li and P. K. Shen, *Adv. Mater.*, 2013, **25**, 2474–2480.
36 D. Lozano-Castelló, D. Cazorla-Amorós, A. Linares-Solano, S. Shiraishi, H. Kurihara and A. Oya, *Carbon*, 2003, **41**, 1765–1775.
37 A. B. Fuertes and M. Sevilla, *Carbon*, 2015, **94**, 41–52.
38 W.-K. Shin, A. G. Kannan and D.-W. Kim, *ACS Appl. Mater. Interfaces*, 2015, **7**, 23700–23707.
39 L. Wei and G. Yushin, *Carbon*, 2011, **49**, 4830–4838.

40 Y. Sun, Q. Wu and G. Q. Shi, *Energy Environ. Sci.*, 2011, **4**, 1113–1132.
41 C. Wang, Z. Guo, W. Shen, Q. Xu, H. Liu and Y. Wang, *Adv. Funct. Mater.*, 2014, **24**, 5511–5521.
42 J. P. Paraknowitsch and A. Thomas, *Energy Environ. Sci.*, 2013, **6**, 2839–2855.
43 L. Zhou, H. Cao, S. Zhu, L. Hou and C. Yuan, *Green Chem.*, 2015, **17**, 2373–2382.
44 G. Hasegawa, T. Deguchi, K. Kanamori, Y. Kobayashi, H. Kageyama, T. Abe and K. Nakanishi, *Chem. Mater.*, 2015, **27**, 4703–4712.
45 M. Nazarian-Samani, S. Haghighat-Shishavan, M. Nazarian-Samani, M.-S. Kim, B.-W. Cho, S.-H. Oh, S. F. Kashani-Bozorg and K.-B. Kim, *J. Power Sources*, 2017, **372**, 286–296.
46 G. Zou, H. Hou, G. Zhao, Z. Huang, P. Ge and X. Ji, *Green Chem.*, 2017, **19**, 4622–4632.
47 A. G. Kannan, A. Samuthirapandian and D.-W. Kim, *J. Power Sources*, 2017, **337**, 65–72.
48 J. Wang and S. Kaskel, *J. Mater. Chem.*, 2012, **22**, 23710–23725.
49 C. Chen, Y. Zhang, Y. Li, J. Dai, J. Song, Y. Yao, Y. Gong, I. Kierzewski, J. Xie and L. Hu, *Energy Environ. Sci.*, 2017, **10**, 538–545.
50 A. Ganesan, R. Mukherjee, J. Raj and M. M. Shaijumon, *J. Porous Mater.*, 2014, **21**, 839–847.
51 S. Rajendiran, P. Natarajan and S. Yoon, *RSC Adv.*, 2017, **7**, 4635–4638.
52 F. Yao, D. T. Pham and Y. H. Lee, *ChemSusChem*, 2015, **8**, 2284–2311.
53 J. Deng, M. Li and Y. Wang, *Green Chem.*, 2016, **18**, 4824–4854.
54 C. Li and G. Q. Shi, *Nanoscale*, 2012, **4**, 5549–5563.
55 A. C. Ferrari, J. C. Meyer, V. Scardaci, C. Casiraghi, M. Lazzeri, F. Mauri, S. Piscanec, D. Jiang, K. S. Novoselov, S. Roth and A. K. Geim, *Phys. Rev. Lett.*, 2006, **97**, 187401.
56 L.-F. Chen, Z.-H. Huang, H.-W. Liang, H.-L. Gao and S.-H. Yu, *Adv. Funct. Mater.*, 2014, **24**, 5104–5111.
57 C. Liu, Z. Yu, D. Neff, A. Zhamu and B. Z. Jang, *Nano Lett.*, 2010, **10**, 4863–4868.
58 J. Hou, C. Cao, X. Ma, F. Idrees, B. Xu, X. Hao and W. Lin, *Sci. Rep.*, 2014, **4**, 7260.
59 R. Thangavel, A. G. Kannan, R. Ponraj, M.-S. Park, H. Choi, D.-W. Kim and Y.-S. Lee, *Adv. Mater. Interfaces*, 2018, 1800472.
60 M. Dahbi, N. Yabuuchi, K. Kubota, K. Tokiwa and S. Komaba, *Phys. Chem. Chem. Phys.*, 2014, **16**, 15007–15028.
61 M. D. Stoller and R. S. Ruoff, *Energy Environ. Sci.*, 2010, **3**, 1294–1301.
62 V. Khomenko, E. Frackowiak and F. Béguin, *Electrochim. Acta*, 2005, **50**, 2499–2506.
63 S. Hu, S. Zhang, N. Pan and Y.-L. Hsieh, *J. Power Sources*, 2014, **270**, 106–112.
64 W. Hsieh, T.-L. A. Horng, H.-C. Huang and H. Teng, *J. Mater. Chem. A*, 2015, **3**, 16535–16543.
65 X. Wu, W. Xing, J. Florek, J. Zhou, G. Wang, S. Zhuo, Q. Xue, Z. Yan and F. Kleitz, *J. Mater. Chem. A*, 2014, **2**, 18998–19004.
66 A. Balducci, *J. Power Sources*, 2016, **326**, 534–540.
67 R. Thangavel, A. G. Kannan, R. Ponraj, X. Sun, D.-W. Kim and Y.-S. Lee, *J. Mater. Chem. A*, 2018, **6**, 9846–9853.
68 A. G. Kannan, J. Zhao, S. G. Jo, Y. S. Kang and D.-W. Kim, *J. Mater. Chem. A*, 2014, **2**, 12232–12239.
69 X.-L. Wu, T. Wen, H.-L. Guo, S. Yang, X. Wang and A.-W. Xu, *ACS Nano*, 2013, **7**, 3589–3597.
70 A. Izadi-Najafabadi, *Adv. Mater.*, 2010, **22**, E235–E241.
71 L. Wei, M. Sevilla, A. B. Fuertes, R. Mokaya and G. Yushin, *Adv. Funct. Mater.*, 2012, **22**, 827–834.
72 Y. Li, Z.-Y. Fu and B.-L. Su, *Adv. Funct. Mater.*, 2012, **22**, 4634–4667.
73 M. Sevilla and A. B. Fuertes, *ACS Nano*, 2014, **8**, 5069–5078.
74 W. Huang, H. Zhang, Y. Huang, W. Wang and S. Wei, *Carbon*, 2011, **49**, 838–843.
75 M. Inagaki, H. Konno and O. Tanaike, *J. Power Sources*, 2010, **195**, 7880–7903.

